

University of Nebraska - Lincoln

DigitalCommons@University of Nebraska - Lincoln

Kenneth Bloom Publications

Research Papers in Physics and Astronomy

10-1-2001

Observation of orbitally excited B mesons in $p\bar{p}$ collisions at \sqrt{s} = 1.8 TeV

T. Affolder

Ernest Orlando Lawrence Berkeley National Laboratory, Berkeley, California

Kenneth A. Bloom

University of Nebraska-Lincoln, kenbloom@unl.edu

Collider Detector at Fermilab Collaboration

Follow this and additional works at: <https://digitalcommons.unl.edu/physicsbloom>



Part of the [Physics Commons](#)

Affolder, T.; Bloom, Kenneth A.; and Collaboration, Collider Detector at Fermilab, "Observation of orbitally excited B mesons in $p\bar{p}$ collisions at \sqrt{s} = 1.8 TeV" (2001). *Kenneth Bloom Publications*. 108.
<https://digitalcommons.unl.edu/physicsbloom/108>

This Article is brought to you for free and open access by the Research Papers in Physics and Astronomy at DigitalCommons@University of Nebraska - Lincoln. It has been accepted for inclusion in Kenneth Bloom Publications by an authorized administrator of DigitalCommons@University of Nebraska - Lincoln.

Observation of orbitally excited B mesons in $p\bar{p}$ collisions at $\sqrt{s}=1.8$ TeV

T. Affolder,²¹ H. Akimoto,⁴³ A. Akopian,³⁶ M. G. Albrow,¹⁰ P. Amaral,⁷ S. R. Amendolia,³² D. Amidei,²⁴ K. Anikeev,²² J. Antos,¹ G. Apollinari,³⁶ T. Arisawa,⁴³ T. Asakawa,⁴¹ W. Ashmanskas,⁷ M. Atac,¹⁰ F. Azfar,²⁹ P. Azzi-Bacchetta,³⁰ N. Bacchetta,³⁰ M. W. Bailey,²⁶ S. Bailey,¹⁴ P. de Barbaro,³⁵ A. Barbaro-Galtieri,²¹ V. E. Barnes,³⁴ B. A. Barnett,¹⁷ M. Barone,¹² G. Bauer,²² F. Bedeschi,³² S. Belforte,⁴⁰ G. Bellettini,³² J. Bellinger,⁴⁴ D. Benjamin,⁹ J. Bensinger,⁴ A. Beretvas,¹⁰ J. P. Berge,¹⁰ J. Berryhill,⁷ S. Bertolucci,¹² B. Bevensee,³¹ A. Bhatti,³⁶ C. Bigongiari,³² M. Binkley,¹⁰ D. Bisello,³⁰ R. E. Blair,² C. Blocker,⁴ K. Bloom,²⁴ B. Blumenfeld,¹⁷ B. S. Blusk,³⁵ A. Bocci,³² A. Bodek,³⁵ W. Bokhari,³¹ G. Bolla,³⁴ Y. Bonushkin,⁵ D. Bortoletto,³⁴ J. Boudreau,³³ A. Brandl,²⁶ S. van den Brink,¹⁷ C. Bromberg,²⁵ M. Brozovic,⁹ N. Bruner,²⁶ E. Buckley-Geer,¹⁰ J. Budagov,⁸ H. S. Budd,³⁵ K. Burkett,¹⁴ G. Busetto,³⁰ A. Byon-Wagner,¹⁰ K. L. Byrum,² M. Campbell,²⁴ A. Caner,³² W. Carithers,²¹ J. Carlson,²⁴ D. Carlsmith,⁴⁴ J. Cassada,³⁵ A. Castro,³⁰ D. Cauz,⁴⁰ A. Cerri,³² A. W. Chan,¹ P. S. Chang,¹ P. T. Chang,¹ J. Chapman,²⁴ C. Chen,³¹ Y. C. Chen,¹ M.-T. Cheng,¹ M. Chertok,³⁸ G. Chiarelli,³² I. Chirikov-Zorin,⁸ G. Chlachidze,⁸ F. Chlebana,¹⁰ L. Christofek,¹⁶ M. L. Chu,¹ S. Cihangir,¹⁰ C. I. Ciobanu,²⁷ A. G. Clark,¹³ M. Cobal,³² E. Cocca,³² A. Connolly,²¹ J. Conway,³⁷ J. Cooper,¹⁰ M. Cordelli,¹² D. Costanzo,³² J. Cranshaw,³⁹ D. Cronin-Hennessy,⁹ R. Cropp,²³ R. Culbertson,⁷ D. Dagenhart,⁴² F. DeJongh,¹⁰ S. Dell'Agnello,¹² M. Dell'Orso,³² R. Demina,¹⁰ L. Demortier,³⁶ M. Deninno,³ P. F. Derwent,¹⁰ T. Devlin,³⁷ J. R. Dittmann,¹⁰ S. Donati,³² J. Done,³⁸ T. Dorigo,¹⁴ N. Eddy,¹⁶ K. Einsweiler,²¹ J. E. Elias,¹⁰ E. Engels, Jr.,³³ W. Erdmann,¹⁰ D. Errede,¹⁶ S. Errede,¹⁶ Q. Fan,³⁵ R. G. Feild,⁴⁵ C. Ferretti,³² I. Fiori,³ B. Flaughner,¹⁰ G. W. Foster,¹⁰ M. Franklin,¹⁴ J. Freeman,¹⁰ J. Friedman,²² Y. Fukui,²⁰ S. Galeotti,³² M. Gallinaro,³⁶ T. Gao,³¹ M. Garcia-Sciveres,²¹ A. F. Garfinkel,³⁴ P. Gatti,³⁰ C. Gay,⁴⁵ S. Geer,¹⁰ D. W. Gerdes,²⁴ P. Giannetti,³² P. Giromini,¹² V. Glagolev,⁸ M. Gold,²⁶ J. Goldstein,¹⁰ A. Gordon,¹⁴ A. T. Goshaw,⁹ Y. Gotra,³³ K. Goulianos,³⁶ H. Grassmann,⁴⁰ C. Green,³⁴ L. Groer,³⁷ C. Grosso-Pilcher,⁷ M. Guenther,³⁴ G. Guillian,²⁴ J. Guimaraes da Costa,²⁴ R. S. Guo,¹ C. Haber,²¹ E. Hafen,²² S. R. Hahn,¹⁰ C. Hall,¹⁴ T. Handa,¹⁵ R. Handler,⁴⁴ W. Hao,³⁹ F. Happacher,¹² K. Hara,⁴¹ A. D. Hardman,³⁴ R. M. Harris,¹⁰ F. Hartmann,¹⁸ K. Hatakeyama,³⁶ J. Hauser,⁵ J. Heinrich,³¹ A. Heiss,¹⁸ B. Hinrichsen,²³ K. D. Hoffman,³⁴ C. Holck,³¹ R. Hollebeek,³¹ L. Holloway,¹⁶ R. Hughes,²⁷ J. Huston,²⁵ J. Huth,¹⁴ H. Ikeda,⁴¹ M. Incagli,³² J. Incandela,¹⁰ G. Introzzi,³² J. Iwai,⁴³ Y. Iwata,¹⁵ E. James,²⁴ H. Jensen,¹⁰ M. Jones,³¹ U. Joshi,¹⁰ H. Kambara,¹³ T. Kamon,³⁸ T. Kaneko,⁴¹ K. Karr,⁴² H. Kasha,⁴⁵ Y. Kato,²⁸ T. A. Keaffaber,³⁴ K. Kelley,²² M. Kelly,²⁴ R. D. Kennedy,¹⁰ R. Kephart,¹⁰ D. Khazins,⁹ T. Kikuchi,⁴¹ M. Kirk,⁴ B. J. Kim,¹⁹ H. S. Kim,¹⁶ M. J. Kim,¹⁹ S. H. Kim,⁴¹ Y. K. Kim,²¹ L. Kirsch,⁴ S. Klimenko,¹¹ P. Koehn,²⁷ A. Königter,¹⁸ K. Kondo,⁴³ J. Konigsberg,¹¹ K. Kordas,²³ A. Korn,²² A. Korytov,¹¹ E. Kovacs,² J. Kroll,³¹ M. Kruse,³⁵ S. E. Kuhlmann,² K. Kurino,¹⁵ T. Kuwabara,⁴¹ A. T. Laasanen,³⁴ N. Lai,⁷ S. Lami,³⁶ S. Lammel,¹⁰ J. I. Lamoureux,⁴ M. Lancaster,²¹ G. Latino,³² T. LeCompte,² A. M. Lee IV,⁹ S. Leone,³² J. D. Lewis,¹⁰ M. Lindgren,⁵ T. M. Liss,¹⁶ J. B. Liu,³⁵ Y. C. Liu,¹ N. Lockyer,³¹ J. Loken,²⁹ M. Loretto,³⁰ D. Lucchesi,³⁰ P. Lukens,¹⁰ S. Lusin,⁴⁴ L. Lyons,²⁹ J. Lys,²¹ R. Madrak,¹⁴ K. Maeshima,¹⁰ P. Maksimovic,¹⁴ L. Malferrari,³ M. Mangano,³² M. Mariotti,³⁰ G. Martignon,³⁰ A. Martin,⁴⁵ J. A. J. Matthews,²⁶ P. Mazzanti,³ K. S. McFarland,³⁵ P. McIntyre,³⁸ E. McKigney,³¹ M. Menguzzato,³⁰ A. Menzione,³² E. Meschi,³² C. Mesropian,³⁶ C. Miao,²⁴ T. Miao,¹⁰ R. Miller,²⁵ J. S. Miller,²⁴ H. Minato,⁴¹ S. Miscetti,¹² M. Mishina,²⁰ N. Moggi,³² E. Moore,²⁶ R. Moore,²⁰ Y. Morita,²⁰ A. Mukherjee,¹⁰ T. Muller,¹⁸ A. Munar,³² P. Murat,³² S. Murgia,²⁵ M. Musy,⁴⁰ J. Nachtman,⁵ S. Nahn,⁴⁵ H. Nakada,⁴¹ T. Nakaya,⁷ I. Nakano,¹⁵ C. Nelson,¹⁰ D. Neuberger,¹⁸ C. Newman-Holmes,¹⁰ C.-Y. P. Ngan,²² P. Nicolaidi,⁴⁰ H. Niu,⁴ L. Nodulman,² A. Nomerotski,¹¹ S. H. Oh,⁹ T. Ohmoto,¹⁵ T. Ohsugi,¹⁵ R. Oishi,⁴¹ T. Okusawa,²⁸ P. Olsen,⁴⁴ C. Pagliarone,³² F. Palmonari,³² R. Paoletti,³² V. Papadimitriou,³⁹ S. P. Pappas,⁴⁵ D. Partos,⁴ J. Patrick,¹⁰ G. Pauletta,⁴⁰ M. Paulini,²¹ C. Paus,²² L. Pescara,³⁰ T. J. Phillips,⁹ G. Piacentino,³² K. T. Pitts,¹⁰ R. Plunkett,¹⁰ A. Pompos,³⁴ L. Pondrom,⁴⁴ G. Pope,²³ M. Popovic,²³ F. Prokoshin,⁸ J. Proudfoot,² F. Ptohos,¹² G. Punzi,³² K. Ragan,²³ A. Rakitine,²² D. Reher,²¹ A. Reichold,²⁹ W. Riegler,¹⁴ A. Ribon,³⁰ F. Rimondi,³ L. Ristori,³² W. J. Robertson,⁹ A. Robinson,²³ T. Rodrigo,⁶ S. Rolli,⁴² L. Rosenson,²² R. Roser,¹⁰ R. Rossin,³⁰ W. K. Sakumoto,³⁵ D. Saltzberg,⁵ A. Sansoni,¹² L. Santi,⁴⁰ H. Sato,⁴¹ P. Savard,²³ P. Schlabach,¹⁰ E. E. Schmidt,¹⁰ M. P. Schmidt,⁴⁵ M. Schmitt,¹⁴ L. Scodellaro,³⁰ A. Scott,⁵ A. Scribano,³² S. Segler,¹⁰ S. Seidel,²⁶ Y. Seiya,⁴¹ A. Semenov,⁸ F. Semeria,³ T. Shah,²² M. D. Shapiro,²¹ P. F. Shepard,³³ T. Shibayama,⁴¹ M. Shimojima,⁴¹ M. Shochet,⁷ J. Siegrist,²¹ G. Signorelli,³² A. Sill,³⁹ P. Sinervo,²³ P. Singh,¹⁶ A. J. Slaughter,⁴⁵ K. Sliwa,⁴² C. Smith,¹⁷ F. D. Snider,¹⁰ A. Solodsky,³⁶ J. Spalding,¹⁰ T. Speer,¹³ P. Sphicas,²² F. Spinella,³² M. Spiropulu,¹⁴ L. Spiegel,¹⁰ L. Stanco,³⁰ J. Steele,⁴⁴ A. Stefanini,³² J. Strologas,¹⁶ F. Strumia,¹³ D. Stuart,¹⁰ K. Sumorok,²² T. Suzuki,⁴¹ R. Takashima,¹⁵ K. Takikawa,⁴¹ M. Tanaka,⁴¹ T. Takano,²⁸ B. Tannenbaum,⁵ W. Taylor,²³ M. Tecchio,²⁴ P. K. Teng,¹ K. Terashi,⁴¹ S. Tether,²² D. Theriot,¹⁰ R. Thurman-Keup,² P. Tipton,³⁵ S. Tkaczyk,¹⁰ K. Tollefson,³⁵ A. Tollestrup,¹⁰ H. Toyoda,²⁸ W. Trischuk,²³ J. F. de Troconiz,¹⁴ S. Truitt,²⁴ J. Tseng,²² N. Turini,³² F. Ukegawa,⁴¹ J. Valls,³⁷ S. Vecjik III,¹⁰ G. Velev,³² R. Vidal,¹⁰ R. Vilar,⁶ I. Vologouev,²¹ D. Vucinic,²² R. G. Wagner,² R. L. Wagner,¹⁰ J. Wahl,⁷ N. B. Wallace,³⁷ A. M. Walsh,³⁷ C. Wang,⁹ C. H. Wang,¹ M. J. Wang,¹ T. Watanabe,⁴¹ D. Waters,²⁹ T. Watts,³⁷ R. Webb,³⁸ H. Wenzel,¹⁸ W. C. Wester III,¹⁰ A. B. Wicklund,² E. Wicklund,¹⁰ H. H. Williams,³¹ P. Wilson,¹⁰ B. L. Winer,²⁷ D. Winn,²⁴ S. Wolbers,¹⁰ D. Wolinski,²⁴ J. Wolinski,²⁵ S. Worm,²⁶ X. Wu,¹³ J. Wyss,³² A. Yagil,¹⁰ W. Yao,²¹ G. P. Yeh,¹⁰ P. Yeh,¹ J. Yoh,¹⁰ C. Yosef,²⁵ T. Yoshida,²⁸ I. Yu,¹⁹ S. Yu,³¹ A. Zanetti,⁴⁰ F. Zetti,²¹ and S. Zucchelli³

(CDF Collaboration)

- ¹*Institute of Physics, Academia Sinica, Taipei, Taiwan 11529, Republic of China*
²*Argonne National Laboratory, Argonne, Illinois 60439*
³*Istituto Nazionale di Fisica Nucleare, University of Bologna, I-40127 Bologna, Italy*
⁴*Brandeis University, Waltham, Massachusetts 02254*
⁵*University of California at Los Angeles, Los Angeles, California 90024*
⁶*Instituto de Fisica de Cantabria, University of Cantabria, 39005 Santander, Spain*
⁷*Enrico Fermi Institute, University of Chicago, Chicago, Illinois 60637*
⁸*Joint Institute for Nuclear Research, RU-141980 Dubna, Russia*
⁹*Duke University, Durham, North Carolina 27708*
¹⁰*Fermi National Accelerator Laboratory, Batavia, Illinois 60510*
¹¹*University of Florida, Gainesville, Florida 32611*
¹²*Laboratori Nazionali di Frascati, Istituto Nazionale di Fisica Nucleare, I-00044 Frascati, Italy*
¹³*University of Geneva, CH-1211 Geneva 4, Switzerland*
¹⁴*Harvard University, Cambridge, Massachusetts 02138*
¹⁵*Hiroshima University, Higashi-Hiroshima 724, Japan*
¹⁶*University of Illinois, Urbana, Illinois 61801*
¹⁷*The Johns Hopkins University, Baltimore, Maryland 21218*
¹⁸*Institut für Experimentelle Kernphysik, Universität Karlsruhe, 76128 Karlsruhe, Germany*
¹⁹*Korean Hadron Collider Laboratory, Kyungpook National University, Taegu 702-701*
Seoul National University, Seoul 151-742, Korea
and SungKyunKwan University, Suwon 440-746, Korea
²⁰*High Energy Accelerator Research Organization (KEK), Tsukuba, Ibaraki 305, Japan*
²¹*Ernest Orlando Lawrence Berkeley National Laboratory, Berkeley, California 94720*
²²*Massachusetts Institute of Technology, Cambridge, Massachusetts 02139*
²³*Institute of Particle Physics, McGill University, Montreal H3A 2T8, Canada*
and University of Toronto, Toronto M5S 1A7, Canada
²⁴*University of Michigan, Ann Arbor, Michigan 48109*
²⁵*Michigan State University, East Lansing, Michigan 48824*
²⁶*University of New Mexico, Albuquerque, New Mexico 87131*
²⁷*The Ohio State University, Columbus, Ohio 43210*
²⁸*Osaka City University, Osaka 588, Japan*
²⁹*University of Oxford, Oxford OX1 3RH, United Kingdom*
³⁰*Universita di Padova, Istituto Nazionale di Fisica Nucleare, Sezione di Padova, I-35131 Padova, Italy*
³¹*University of Pennsylvania, Philadelphia, Pennsylvania 19104*
³²*Istituto Nazionale di Fisica Nucleare, University and Scuola Normale Superiore of Pisa, I-56100 Pias, Italy*
³³*University of Pittsburgh, Pittsburgh, Pennsylvania 15260*
³⁴*Purdue University, West Lafayette, Indiana 47907*
³⁵*University of Rochester, Rochester, New York 14627*
³⁶*Rockefeller University, New York, New York 10021*
³⁷*Rutgers University, Piscataway, New Jersey 08855*
³⁸*Texas A&M University, College Station, Texas 77843*
³⁹*Texas Tech University, Lubbock, Texas 79409*
⁴⁰*Istituto Nazionale di Fisica Nucleare, University of Trieste/Udine, Italy*
⁴¹*University of Tsukuba, Tsukuba, Ibaraki 305, Japan*
⁴²*Tufts University, Medford, Massachusetts 02155*
⁴³*Waseda University, Tokyo 169, Japan*
⁴⁴*University of Wisconsin, Madison, Wisconsin 53706*
⁴⁵*Yale University, New Haven, Connecticut 06520*

(Received 3 November 1999; revised manuscript received 4 May 2001; published 4 September 2001)

We measure the relative rate of production of orbitally excited ($L=1$) states of B mesons (B^{**}) by observing their decays into $B\pi^\pm$. We reconstruct B mesons through semileptonic decay channels using data collected in $p\bar{p}$ collisions at $\sqrt{s}=1.8$ TeV. The fraction of light B mesons that are produced as $L=1 B^{**}$ states is measured to be $0.28 \pm 0.06(\text{stat}) \pm 0.03(\text{syst})$. We also measure the collective mass of the B^{**} states, and quantify the result by quoting the (model-dependent) mass of the lowest B^{**} state to be $m(B_1)=5.71 \pm 0.02 \text{ GeV}/c^2$.

I. INTRODUCTION

The label “ B^{**} ” is a collective name for the four lowest-lying $L=1$ states of B mesons. The low-lying part of the B meson spectrum is illustrated in Fig. 1. As a result of heavy-quark effective theory (HQET) [1], the heavy quark decouples from the light degrees of freedom in the $m_b \rightarrow \infty$ limit, and thus the B^{**} states are usually labeled by the total angular momentum j of the light quark q , i.e., $\mathbf{J}_q = \mathbf{L} \oplus \mathbf{S}_q$. For the $L=1$ states, this results in two doublets: B_0^* and B_1^* for $j_q = \frac{1}{2}$, and B_1 and B_2^* for $j_q = \frac{3}{2}$. The states within each doublet should be degenerate in mass by HQET and have the same total strong-interaction width. The $1/m_b$ corrections turn out to be significant and break this degeneracy. The states in the $j_q = \frac{1}{2}$ doublet are expected to be broad since they can decay through an S -wave transition, whereas the $j_q = \frac{3}{2}$ states decay through a D -wave transition and are therefore thought to be narrow.

The motivation for studying the B^{**} states is twofold. First, the combination of a heavy and a light quark is the closest QCD analogue of the hydrogen system in QED and is therefore an interesting testing ground for nonperturbative theoretical models. Second, the B^{**} states are expected to decay strongly into $B\pi^\pm$, so the charge of the pion from their decay can be used to determine the flavor of the weakly decaying b quark at the time of its production. By “flavor” we mean whether the bottom quark involved is a b or \bar{b} quark, the common terminology adopted in B^0 mixing and CP-violation studies. This mechanism contributes to the B flavor-tagging technique proposed in Ref. [2] and successfully employed in Refs. [3–6].

Early theoretical predictions [7] of the masses and the widths for these states were obtained by extrapolation from the measured properties of other heavy-light quark systems based on the gross features of heavy-quark symmetry [1]. Calculations in the nonrelativistic valence-quark approximation [8] and the fully relativistic light-quark model [9] have also become available. The latter model is in good agreement with the properties of the observed heavy-light mesons and heavy quarkonia. The predictions of the three approaches are listed in Table I. To date the B^{**} states have been observed only in the e^+e^- environment at LEP [10–13] with properties in reasonable agreement with the expectations.

In this paper we present a measurement of the production rate and the mass of the B^{**} states using a sample of B mesons partially reconstructed through their semileptonic decays into charm mesons. The data were collected with the Collider Detector at Fermilab (CDF) at the Tevatron $p\bar{p}$ collider. This analysis is closely related to that of Ref. [5], and a number of results presented there are not repeated here.

The remainder of this paper is organized as follows: Sec. II gives a brief overview of the CDF detector and the details of data selection and B^{**} reconstruction; Sec. III lists the backgrounds to the B^{**} signal; Sec. IV A explains the fitting procedure and links in the treatment of the most important backgrounds; the results and estimated uncertainties are presented in Sec. IV B; and finally Sec. V contains a summary.

II. THE CDF DETECTOR AND DATA SELECTION

A. Apparatus

This analysis was performed on the data collected with the CDF at the Tevatron collider during the 1992–1996 data-taking period. The integrated luminosity of this data sample is 110 pb^{-1} of $p\bar{p}$ collisions at $\sqrt{s} = 1.8 \text{ TeV}$. A full description of the detector can be found in Refs. [14], [15]. Here we describe briefly only the subsystems relevant to the analysis.

We use a cylindrical coordinate system with the z axis pointing along the beam direction. The polar angle θ is measured from the direction of the proton beam, and the azimuthal angle ϕ from the horizontal plane. The pseudorapidity, $\eta = -\ln[\tan(\theta/2)]$, is frequently used in place of the polar angle. Some quantities are measured only in the plane transverse to the beam line; these are denoted with the subscript “ T ,” e.g., $p_T = p \sin \theta$ is the transverse momentum of a particle and $E_T = E \sin \theta$ its transverse energy.

The tracking systems are located inside a superconducting solenoid, which generates a 1.4 T magnetic field. The silicon vertex detector (SVX) [15] is a solid-state tracking device located immediately outside the beam pipe. It consists of four layers of silicon microstrip detectors at radii ranging from 3.0 to 7.9 cm. The SVX provides a measurement of the impact parameter of tracks in the plane transverse to the beam axis with a resolution of $\sigma_d = (13 + 40/p_T) \mu\text{m}$, where p_T is in GeV/c ; it does not measure the longitudinal coordinates of tracks. The outermost tracking device is the central tracking chamber (CTC), a drift chamber providing a three-dimensional measurement of tracks in the region $|\eta| < 1.1$ from the nominal $p\bar{p}$ interaction point. The combined SVX-CTC system enables us to measure transverse track momenta with the resolution $\delta p_T/p_T \approx \sqrt{(0.9p_T)^2 + (6.6)^2} \times 10^{-3}$, where p_T is in GeV/c . Between the SVX and the CTC lies a set of time-projection chambers measuring the longitudinal positions of the $p\bar{p}$ interaction vertices.

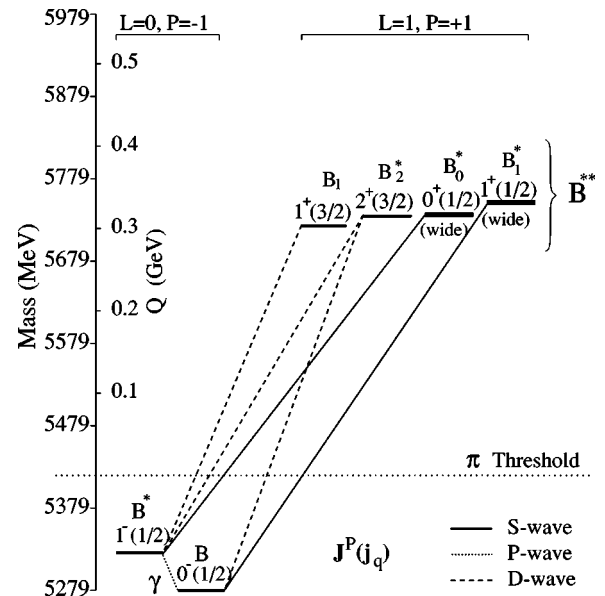


FIG. 1. Predicted spectrum and dominant decays of the low-lying B meson states.

TABLE I. Predicted properties of B^{**} mesons.

Name	J	j_q	Mass (GeV/ c^2)			Width	Decays
			Ref. [7]	Ref. [8]	Ref. [9]		
B_0^*	0	$\frac{1}{2}$		5.870	5.738	broad	$(B\pi)_{L=0}$
B_1^*	1	$\frac{1}{2}$		5.875	5.757	broad	$(B^*\pi)_{L=0}$
B_1	1	$\frac{3}{2}$	5.759	5.700	5.719	narrow	$(B^*\pi)_{L=2}$
B_2^*	2	$\frac{3}{2}$	5.771	5.715	5.733	narrow	$(B\pi, B^*\pi)_{L=2}$

The calorimeters are situated outside the solenoid, and consist of “towers” pointing to the interaction region. Each tower covers 15° in ϕ and 0.1 in η . The central electromagnetic calorimeter ($|\eta| < 1.1$) is an 18 radiation length lead-scintillator stack with a proportional chamber for measurement of the transverse shower profile. Its position resolution is about 2 mm, and the energy resolution is $\delta E_T/E_T = \sqrt{(13.5\%/\sqrt{E_T})^2 + (2\%)^2}$, where E_T is in GeV. Outside it is the iron scintillator central hadronic calorimeter, which is 4.5 interaction lengths thick and provides measurements with a resolution $\delta E_T/E_T = \sqrt{(50\%/\sqrt{E_T})^2 + (3\%)^2}$, where E_T is again in GeV.

The central muon chambers (CMU’s) are located outside the calorimeters and cover the region $|\eta| < 0.6$ with 85% coverage in ϕ . Beyond the CMU there is an additional absorber of 60 cm of steel followed by the central muon upgrade chambers (CMP’s) ($|\eta| < 0.6$ with 65% coverage). Both are made up of four layers of drift chambers.

The CDF detector has a three-level triggering system. The first two levels are hardware triggers, and the third is a software trigger derived from the off-line reconstruction code. The events used in this analysis satisfied triggers that require either an electron of high energy (calorimeter deposition above $E_T \sim 8$ GeV and an associated track above $p_T \sim 7.5$ GeV/ c) or a muon of high momentum (p_T above ~ 7.5 GeV/ c).

For the simulation needs of this analysis, we use the PYTHIA 5.7/JETSET 7.4 generator [16] with several of its parameters adjusted to achieve a good description of charged-particle multiplicities of $b\bar{b}$ events produced in $p\bar{p}$ collisions. The tuning procedure is summarized in Sec. III B 1. This analysis is, however, not particularly sensitive to the tuning. The generated B mesons are decayed using the the CLEO QQ B -decay Monte Carlo program [17], and the result-

ing events passed through the standard CDF detector simulation.

B. Data selection

1. B candidate selection

We search for the semileptonic decay of B mesons into an electron or muon (which is the basis of the trigger), a neutrino, and a $D^{(*)}$ meson. The $D^{(*)}$ is reconstructed in several hadronic decay modes. The topology of a representative semileptonic B decay is shown in Fig. 2. We reconstruct the following “decay signatures” for our B meson samples:¹

- (a) $B^+ \rightarrow \nu l^+ \bar{D}^0$, $\bar{D}^0 \rightarrow K^+ \pi^-$,
- (b) $B^+ \rightarrow \nu l^+ \bar{D}^0$, $\bar{D}^0 \rightarrow K^+ \pi^- \pi^+ \pi^-$,
- (c) $B^0 \rightarrow \nu l^+ D^-$, $D^- \rightarrow K^+ \pi^- \pi^-$,
- (d) $B^0 \rightarrow \nu l^+ D^{*-}$, $D^{*-} \rightarrow \bar{D}^0 \pi_s^-$, $\bar{D}^0 \rightarrow K^+ \pi^-$,
- (e) $B^0 \rightarrow \nu l^+ D^{*-}$, $D^{*-} \rightarrow \bar{D}^0 \pi_s^-$, $\bar{D}^0 \rightarrow K^+ \pi^- \pi^+ \pi^-$,
- (f) $B^0 \rightarrow \nu l^+ D^{*-}$, $D^{*-} \rightarrow \bar{D}^0 \pi_s^-$, $\bar{D}^0 \rightarrow K^+ \pi^- \pi^0$,

where the pion from the D^{*-} decay is denoted as π_s^- to distinguish it from others in the decay sequence. We refer to each of these as a “decay signature” since they represent the experimental selection process, which in turn results in subsamples that are not exclusively composed of the listed sequence of decays. One decay chain of a B meson may mimic another if particles are missed in the reconstruction. For example, the B^0 decay sequence written for signature (d) will contribute to the event subsample of (a) if the π_s^- from the D^{*-} decay fails the reconstruction criteria. In general, if a charged particle is missed in the reconstruction, the apparent B charge is changed, and charged and neutral B mesons will thereby cross contaminate each other’s signatures. The contamination between charged and neutral B mesons is relatively modest, not more than 20% for any of the signatures in this analysis. The separation is aided by the fact that the first two signatures of $l^+ \bar{D}^0$ have candidates removed if they are also valid $l^+ D^{*-}$ candidates.

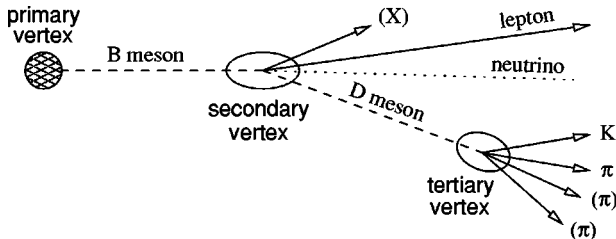


FIG. 2. Topology of a semileptonic B decay. Measurable particles are shown as solid lines. The particles “(X)” originating at the secondary vertex may come from the decays of excited states of D mesons or from $B \rightarrow \nu l D X$ decays.

¹Use of specific particle states in this paper implies the use of the charge-conjugate states as well.

TABLE II. Event selection criteria for the six decay signatures. The cut on the impact parameter significance d_0/σ_0 is applied to D daughter tracks only. $L_{xy}(D)/\sigma_{L_{xy}}$ is the transverse D decay length significance relative to the primary vertex, while ct_D is the proper decay length of the D with respect to the B vertex. $\Delta m(D^*)$ is the mass difference between the D^* candidate and the D candidate plus the charged pion mass.

Selection cuts		Decay signatures					
		$l\bar{D}^0$		lD^-	lD^{*-}		
		$K^+\pi^-$	$K^+\pi^-\pi^+\pi^-$	$K^+\pi^-\pi^-$	$K^+\pi^-$	$K^+\pi^-\pi^+\pi^-$	$K^+\pi^-\pi^0$
$p_T(l) >$	(GeV/ c)	6.0	6.0	6.0	6.0	6.0	6.0
$p_T(K) >$	(GeV/ c)	0.7	0.8	0.6	1.0
$p_T(\pi) >$	(GeV/ c)	0.5	0.6	0.8
$p_T(D) >$	(GeV/ c)	2.0	3.0	3.0
$d_0/\sigma_0 >$		3.0	...	2.0	1.0	0.5	1.0
$L_{xy}(D)/\sigma_{L_{xy}} >$		3.0	3.0	5.0	1.0	1.0	1.0
$ \Delta m(D^*) <$	(MeV/ c^2)	3.0	2.0	...
$m(lD) <$	(GeV/ c^2)	5.0	5.0	5.0
$-0.5 < ct_D <$	(mm)	1.0	1.0	2.0	1.0	1.0	1.5
$ m(\pi^+\pi^-) - m(\rho^0) <$	(GeV/ c^2)	...	0.15
$ m(K^+\pi^-) - 1.5 <$	(GeV/ c^2)	0.2

The sample selection is the same as Ref. [5] except for the addition of the $l^+\bar{D}^0$, $\bar{D}^0 \rightarrow K^+\pi^-\pi^+\pi^-$ signature, which increased the sample of charged B mesons by nearly 60%. The reader may refer to this previous work for details of the B candidate selection; we only outline the approach here and summarize the kinematic and geometric selection criteria in Table II.

The tracks of the $D^{(*)}$ daughters must lie within a cone of $\Delta R \equiv \sqrt{(\Delta\eta)^2 + (\Delta\phi)^2} = 1.0$ around the lepton, and exceed a p_T threshold (see Table II). All tracks (except one in the case of $D^0 \rightarrow K^+\pi^-\pi^-\pi^+$) must use SVX information, and they must also be consistent with originating in the vicinity of the same primary vertex. The candidate tracks must form a mass in a loose window around the nominal D mass, where all permutations of mass assignments, consistent with the charm hypothesis, are attempted. The candidate tracks are then combined in a fit constraining them to a D decay vertex, and χ^2 and mass window cuts are imposed. We require the D tracks to be displaced from the primary vertex based on the track impact parameter significance d_0/σ_0 , where d_0 is the impact parameter in the transverse plane with respect to the primary vertex and σ_0 is its error. The specific requirement depends upon the decay signature, as listed in Table II. The projected transverse distance $L_{xy}(D)$ between the D vertex and the primary vertex must be greater than its uncertainty $\sigma_{L_{xy}}$ [$L_{xy}(D)/\sigma_{L_{xy}}$ cut in Table II]. We next find the B vertex by projecting the D back to the lepton track, and their intersection determines the B vertex, as sketched in Fig. 2. If the reconstruction includes a π_s^- from a D^{*-} decay, the π_s^- is used to further constrain the B vertex. A loose cut is applied to the D proper decay length relative to the B vertex (ct_D cut in Table II). Some further demands on masses or mass differences are summarized in Table II. Finally, the lepton and the charm candidates are required to be consistent with the

decay of a single B , i.e., the signal must have a l^+K^+ or l^-K^- correlation.

Figure 3 shows the charm candidate mass distributions for the six reconstructed B signatures. The solid (dashed) histograms in the figure are the distributions of the candidates with the right (wrong) $l-K$ charge correlation coming from a single B meson. The wrong-sign distributions show no excess at the appropriate charm mass, indicating that the right-sign distributions are clean samples of semileptonic B decays. The numbers of B candidates for each decay signature, summarized in Table III, are determined by sideband (hatched regions in Fig. 3) subtraction. This is a straightforward procedure except for the $\bar{D}^0 \rightarrow K^+\pi^-\pi^0$ signature (f), where we use the shape of the wrong-sign mass difference distribution (dashed histogram) renormalized to the (hatched) right-sign sideband region. The selections result in a total of almost 10 000 partially reconstructed B mesons.

2. B^{**} candidate reconstruction

A B^{**} candidate is constructed by combining a B candidate with any track compatible with originating from the primary interaction vertex—generally referred to as a “prompt” track. We assume that every such track was produced by a pion since we do not efficiently distinguish particle species. The tracks are required to be reconstructed in the SVX for precision measurement of the impact parameter, and have an impact parameter that is less than 3.0 standard deviations from the primary vertex. Furthermore, only tracks with transverse momentum greater than 900 MeV/ c are used. This value was determined from the Monte Carlo simulations in order to maximize the significance of the anticipated B^{**} signal.

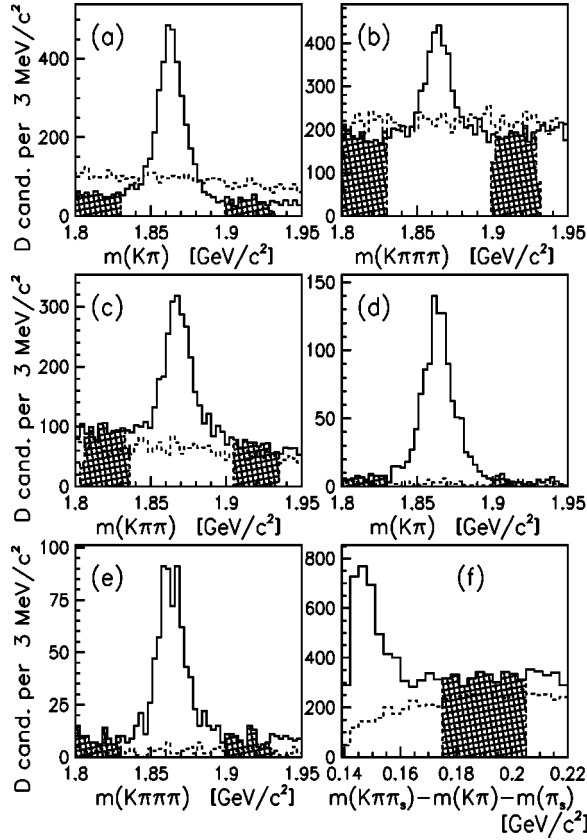


FIG. 3. Mass distributions of the $D^{(*)}$ candidates for the six B decay signatures (see the text for the alphabetical signature labels). The last signature (f) is for $\bar{D}^0 \rightarrow K^+ \pi^- \pi^0$, where the π^0 is not part of the reconstruction, and the mass difference between the visible D^{*-} and \bar{D}^0 decay products is plotted instead of the mass. The solid histograms are for the candidates that have the correct charge correlation for B decays ($l^\pm K^\pm$), and the dashed histograms for the opposite correlation. The hatched regions are the sidebands used for background subtraction. The yields of B mesons are summarized in Table III.

The missing neutrino from the semileptonic B decay prevents us from fully reconstructing the B meson.² Our resolution on the mass of the B^{**} candidates is thereby impaired by the unknown momentum of the neutrino. The kinematics of the B meson decays in our sample are determined mostly by the acceptance of the lepton triggers and, to a lesser extent, by the selection requirements on the hadronic D decay products. The relatively high momentum threshold of the lepton triggers biases the neutrinos of those B mesons entering our sample to possess a fairly modest fraction of the full B momentum. As a result, on average, the reconstructed B decay products comprise about 85% of the true B momentum (average B transverse momentum is ~ 21 GeV/ c), and have an rms spread about the mean of $\sim 10\%$.

The mass resolution of the reconstructed B^{**} candidates can be improved by correcting the measured momentum of the visible B decay products to account for the loss of the neutrino. An average multiplicative correction factor for each decay signature, determined by Monte Carlo simulation, is applied on an event-by-event basis to the momentum of the reconstructed B candidate as a function of the mass of the visible B decay products. Instead of using the direction of the visible B momentum, the transverse direction of the B meson is deduced from the B production and decay vertices for a further improvement in the B^{**} mass resolution.

Despite these corrections, the smearing of the B^{**} candidate masses, due to the missing neutrino, is still severe. Instead of looking for a $B^{**} \rightarrow B \pi^\pm$ peak in the mass distribution, we use the mass difference $Q \equiv m(B \pi) - m(B) - m(\pi)$, where the reconstructed mass of the B candidates is used. Some of the smearing effects within an event cancel for this quantity. The resolution of Q is, however, also affected by the decays of the B^{**} to B^* , since we do not reconstruct the soft photon from $B^* \rightarrow B \gamma$. Furthermore, only two of the B^{**} states are expected to be narrow (~ 20 MeV/ c^2), while the other two, making up one third of all B^{**} states by spin counting, should be broad (~ 100 MeV/ c^2) [7]. Monte Carlo studies indicate that the

TABLE III. The numbers of B candidates in the signal regions and the estimated numbers of B mesons after background subtraction for each decay signature.

Signature	Candidates	B mesons
(a) $\bar{D}^0 \rightarrow K^+ \pi^-$	3141	2668 ± 53
(b) $\bar{D}^0 \rightarrow K^+ \pi^- \pi^+ \pi^-$	3404	1534 ± 49
B^+ signatures total	6545	4202 ± 73
(c) $D^- \rightarrow K^+ \pi^- \pi^-$	2275	1454 ± 43
(d) $D^{*-} \rightarrow \bar{D}^0 \pi_s^-, \bar{D}^0 \rightarrow K^+ \pi^-$	891	835 ± 29
(e) $D^{*-} \rightarrow \bar{D}^0 \pi_s^-, \bar{D}^0 \rightarrow K^+ \pi^- \pi^+ \pi^-$	618	524 ± 23
(f) $D^{*-} \rightarrow \bar{D}^0 \pi_s^-, \bar{D}^0 \rightarrow K^+ \pi^- \pi^0$	4288	2678 ± 59
B^0 signatures total	8072	5491 ± 82

²The B decay signatures include contributions from $B \rightarrow \nu l D^{**}$ decays, for which the pion or photon from the D^{**} decay chain is also missing. The kinematic effects of these other missing particles are implicitly included when referring to the “neutrino,” which is usually the dominant source of missing momentum.

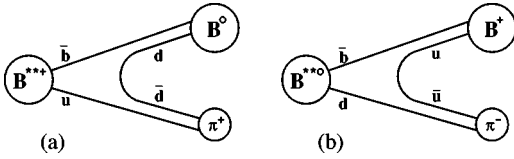


FIG. 4. An idealized picture of the decays of B^{**} mesons into B mesons and charged pions illustrating the pion charge correlations with the constituent quark types.

resolution of Q for B^{**} decays, in spite of these resolution-limiting effects, is around $50 \text{ MeV}/c^2$ with no significant systematic shift after correcting the visible B momentum.

The charge of the pion from a B^{**} decay always matches the light quark content of the associated B meson, i.e., B^{**} mesons decay into $B^+\pi^-$ or $B^0\pi^+$, as shown in Fig. 4, and never to $B^+\pi^+$ or $B^0\pi^-$. We label the correct $B^+\pi^-$ and $B^0\pi^+$ pairings as “right sign,” and the unphysical decay combination as “wrong sign.” It is important to note that B mesons with the same b flavor (e.g., B^+ and B^0) have the *opposite* definition for the right-sign pion charge, i.e., π^+ for B^0 and π^- for B^+ . If one knew, without fail, the flavor and charge state of the B meson at the time of creation, the B^{**} would appear as an excess in the right-sign Q distributions only. In our sample, however, we expect some cross contamination between flavors through $B^0-\bar{B}^0$ oscillations and incomplete reconstruction of all of the B decay products, as explained later in the paper.

A further complication is present. The particles produced in the hadronization of b quarks into B mesons are also expected to form low-mass combinations with the B candidates, and to favor the same right-sign correlation as in B^{**} decays. Thus, the primary experimental difficulty in this analysis is to separate the (broad) resonant B^{**} signal from the low-mass nonresonant hadronization background, which also favors the same right-sign charge correlation.

The Q distributions of our $B\pi^\pm$ candidates are shown in Fig. 5. These are *inclusive* distributions, meaning that we do not choose only one candidate track per B , otherwise biases may be introduced that are difficult to calculate. Any track that satisfies our selection criteria enters into these distributions, so there may be multiple B^{**} candidates per B candidate. There is a clear right-sign excess at low Q , but as alluded to above, the background (e.g., wrong-sign candidates) peak in the same region, and the behavior is quite different for the charged and neutral signatures. We next consider the various contributions to Fig. 5, and disentangle the B^{**} signal from the charge correlated and kinematically similar hadronization background in the data.

III. B^{**} BACKGROUNDS

The backgrounds to a potential B^{**} signal can be divided into two broad classes. We refer to those produced in association with the b quark, and which are therefore dependent on its charge and momentum, as “correlated” backgrounds. Those that are independent of the presence of heavy quarks in the event are “uncorrelated” backgrounds. We sideband subtract the uncorrelated backgrounds directly in the data,

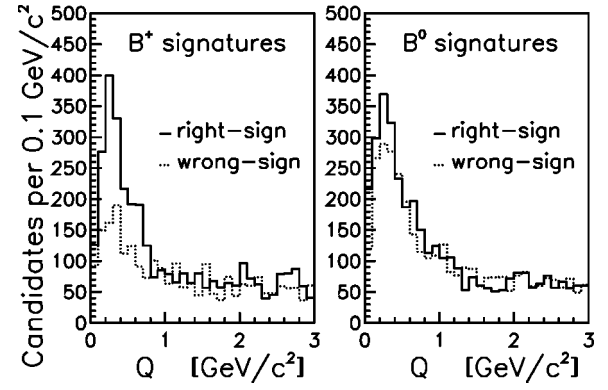


FIG. 5. The Q distributions of the $B\pi^\pm$ candidates in the data summed over the charged (left) and neutral (right) B signatures. The candidates with the right (wrong) $B-\pi^\pm$ charge correlation are shown as solid (dashed) histograms.

whereas the correlated ones, especially the one coming from hadronization tracks around the B meson, require a more involved treatment.

A. Uncorrelated backgrounds

Three sources of uncorrelated background contributions are taken into account: fake B meson candidates, “pile-up” events, and particles from the “underlying” event. All three components are measured from the same data sample that is used for this analysis, and their contributions are subtracted before the $B-\pi$ candidates are analyzed further.

The combinatorial background in the reconstruction of the $D^{(*)}$ mesons results in fake B meson candidates under the $D^{(*)}$ mass peaks. We divide the mass spectrum of $D^{(*)}$ candidates into signal and sideband regions (shown in Fig. 3), and perform a sideband subtraction on the Q distribution of the B^{**} candidates. This subtraction is performed independently for each B meson signature. This procedure yields the $B-\pi$ Q distributions for true B mesons, but there are other backgrounds to a B^{**} signal that must be considered.

At the higher Tevatron luminosities, it is not unusual to have multiple hard $p\bar{p}$ collisions in the same beam crossing, which we refer to as event “pile up.” The spatial resolution of the tracking detectors is on the order of a centimeter along the beam (z) axis, whereas the collisions have a corresponding $\sim 30 \text{ cm}$ rms spread around the center of the detector. It is usually possible to distinguish which tracks arise from which interaction, but occasionally a secondary collision will occur so close in z to the one that produced the B meson that the two cannot be distinguished. In the latter case, we will sometimes form B^{**} candidates using pions from $p\bar{p}$ interactions unrelated to the one that produced the B meson.

We correct for this effect by looking at the distribution of tracks well separated from the B vertex and then extrapolate into the region where we are unable to resolve additional vertices close to the B . We first determine the distribution of the spatial separations (Δz) along the beam line between the B production vertex and the z coordinate of tracks in the event (i.e., the z coordinate of the point of closest approach

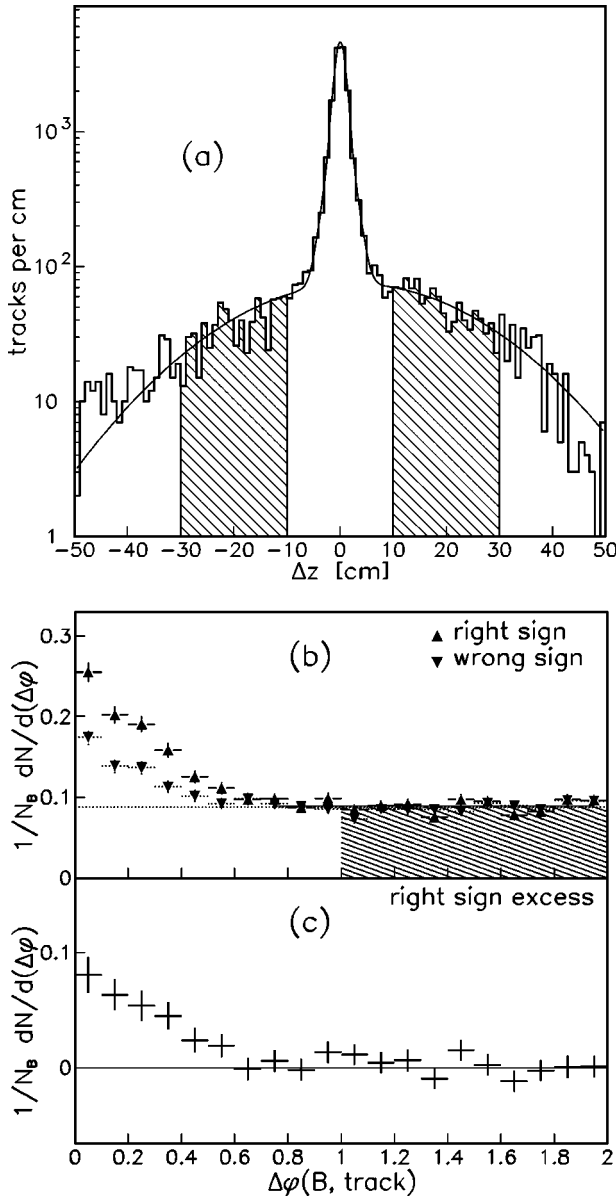


FIG. 6. Background track distributions: (a) The Δz distribution between the B meson's production vertex and other tracks in the event for data (histogram), and a parametrized fit to the data (solid curve). (b) The azimuthal distribution $\Delta\phi$ of tracks with respect to the B meson direction for $|\Delta\eta| < 1$, right- and wrong-sign $B-\pi$ pairs, are plotted separately. (c) The azimuthal distribution for the right-sign excess.

of the track helix to the beam line). This distribution, shown in Fig. 6(a), has a narrow peak at $\Delta z = 0$ that is composed of tracks coming from the same interaction as the B meson and that has a width characteristic of the z resolution of the detector. This peak lies on top of a broad Gaussian-like distribution of tracks coming from other (uncorrelated) $p\bar{p}$ interactions in the same beam crossing. From the fitted curves in Fig. 6(a), the pile-up background accounts for about 5% of the total tracks we associate with the B production vertex in the B^{**} reconstruction. We define a signal region ($|\Delta z| < 5$ cm) and choose sidebands [hatched regions in Fig. 6(a)]

to produce a Δz sideband subtracted Q distribution of the $B-\pi$ candidates.

The final uncorrelated background component we take into account is that from the particles of the “underlying event.” In most $p\bar{p}$ collisions, any heavy flavor produced accounts for only a fraction of all particles emanating from the collision. The remaining particles are the product of radiation of the remnants of the original (anti)proton. These particles are expected to be uncorrelated with the direction of the b jets, and therefore isotropic in the plane transverse to the beam. We tested this assumption by verifying that the azimuthal distribution of particles relative to the reconstructed B meson over $0 < |\phi(\text{track}) - \phi(B)| < 2$ is uniform in the $|\Delta\eta| \equiv |\eta(\text{track}) - \eta(B)| > 1$ region.³

We correct for this underlying track background by again doing a variant of the sideband-subtraction procedure. The distribution of azimuthal separations between charged particles and the reconstructed B mesons with $|\Delta\eta| < 1$, shown in Fig. 6(b), reveals that most of the b jet associated with the B meson is confined to the region $|\Delta\phi| < 0.8$. One sees from Fig. 6(c), consistent with this observation, that the right wrong-sign asymmetry vanishes outside this “ B ” region of $|\Delta\phi| < 0.8$. The uniform distribution in the $1 < |\Delta\phi| < 2$ region is presumed to be dominated by the underlying event particles, and we use the properties of these tracks to estimate the contribution of the underlying event particles to the Q distribution. This is accomplished by rotating these tracks [hatched “sideband” in Fig. 6(b)] in the transverse plane “under” the B meson, i.e., reducing their $|\Delta\phi|$ by 1. We then subtract the Q distribution of these “sideband” events from the raw $B-\pi$ Q distribution to remove the effect of the underlying event background from the B^{**} candidates.

The Q distribution of the B^{**} candidates, which results after these three backgrounds have been subtracted from the raw distribution (Fig. 5) is shown in Fig. 7. A clear right-sign excess remains, but one still may not interpret this excess as a B^{**} signal.

B. Correlated backgrounds

The corrected Q distributions in Fig. 7 consist predominantly of combinatoric background formed from real B mesons combined with hadronization particles from the formation of the B meson, and the (potential) B^{**} signal. The main difficulty in this analysis lies in making a robust distinction between these two components as they both have similar kinematic characteristics and a preference for the right-sign $B-\pi$ correlation. We use a Monte Carlo inspired parametrization, constrained by the data, as a model for the Q distribution of the hadronization background. This approach to modeling the hadronization background is found to be fairly insensitive to the details of the simulation.

³We restrict the azimuthal range because the uniformity is spoiled as $|\Delta\phi|$ approaches π by the tracks coming from the jet associated with the other b hadron in the event. This other jet tends to be back-to-back in ϕ with respect to the B meson, but is largely uncorrelated to it in η .

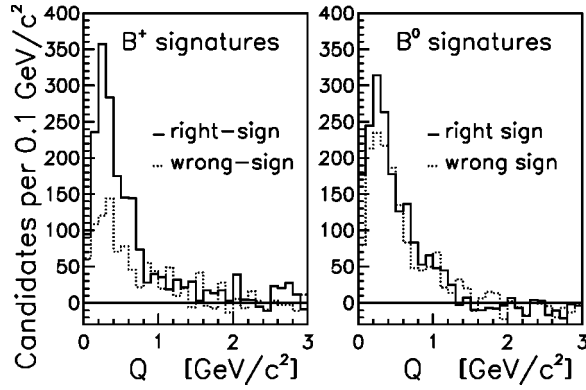


FIG. 7. The Q distributions of the $B\pi^\pm$ candidates in the data after the subtraction of the uncorrelated backgrounds from the raw distributions of Fig. 5.

1. Hadronization particles

Hadronization particles are those resulting from the QCD processes that form a color-neutral meson from a b quark. All the B^{**} analyses published to date [10–13] rely on Monte Carlo calculations to predict the shapes of either Q or mass distributions [i.e., $n(Q) \equiv dN/dQ$ or dN/dm] for this background. We found that the available Monte Carlo event generators poorly describe the complex environment of a hadron collider in this respect. For this reason we sought to constrain the shape of this background from the data and thereby reduce the dependence of the results on the hadronization model implemented in a given simulation.

A simple approach would be to parametrize the shape of the Q distribution arising from the hadronization tracks, fit the parametrization to the wrong-sign $B\pi$ combinations [$n_{\text{WS}}(Q)$] of Fig. 7, and subtract the same distribution from the right-sign candidates [$n_{\text{RS}}(Q)$]. This is, however, incorrect since one does not expect the right-sign and the wrong-sign hadronization components to have the same magnitude.

A mechanism believed to be responsible for such a difference is illustrated in Fig. 8: as a \bar{b} quark hadronizes, it “pulls” quark-antiquark pairs out of the vacuum, and the first charged pion in the hadronization chain carries a charge correlated with the flavor of the bottom quark. This is the same correlation present in B^{**} decays, namely, $B^+\pi^-$ and $B^0\pi^+$. Pions that form as direct (or near direct) neighbors to the B meson in the (naïve) hadronization chain are expected to have velocities similar to the B , and they will thus preferentially result in $B\pi$ pairs with low Q values similar to B^{**} decays. While this simple qualitative argument does not encompass the full complexity of the hadronization process, the expected correlation trends have been observed in data by

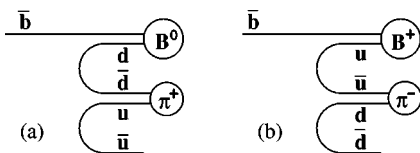


FIG. 8. A simplified picture of the hadronization mechanism that results in a flavor-charge correlation of B mesons and associated charged pions.

several experiments [3–5,10].⁴ One must, therefore, carefully correct the observed Q distributions for the hadronization excess of right-sign over wrong-sign particles.

In dealing with the hadronization background, it is convenient to change variables from the right- and wrong-sign distributions, $n_{\text{RS}}(Q)$ and $n_{\text{WS}}(Q)$, to an equivalent set of variables: the total distribution $n(Q) = n_{\text{RS}}(Q) + n_{\text{WS}}(Q)$ and the correlation asymmetry

$$\mathcal{A}(Q) \equiv \frac{n_{\text{RS}}(Q) - n_{\text{WS}}(Q)}{n_{\text{RS}}(Q) + n_{\text{WS}}(Q)}. \quad (1)$$

The asymmetry of B^{**} decays would be +1 in a sample of known B flavor. Background components uncorrelated with the B mesons have zero asymmetry, but the hadronization background does not.

Since we do not have access to pure hadronization spectra in the data, we must resort to Monte Carlo simulation for guidance in predicting the asymmetries of the hadronization particles, $\mathcal{A}^{\text{HA}}(Q)$. We use the PYTHIA/JETSET program for this purpose. A comparison of this simulation to $p\bar{p}$ data, however, reveals a large discrepancy in the distribution of particle multiplicities as a function of transverse momentum, which can be ascribed to a poor description of the underlying event by the simulation. In order to reduce our dependence on the specific hadronization model employed in the simulation, we adjust the PYTHIA generation parameters such that we obtain a good description of particle distributions. The simulation results are compared to the $l^+\bar{D}^0$, $\bar{D}^0 \rightarrow K^+\pi^-$ data in terms of the charged particle multiplicity distributions as a function of p_T and, with respect to the B meson, ΔR and $\Delta\phi$. PYTHIA parameters governing the underlying event are first tuned to obtain good agreement in a region “away” from the B meson ($1 < \Delta R < 2$), after which hadronization parameters are adjusted to describe the distributions near the B meson ($\Delta R < 0.6$). The values of the “tuned” PYTHIA parameters can be found in Ref. [5], and a full description of the procedure is in Ref. [18].

While the tuning procedure reduces our dependence on the simulation, there nevertheless remains an uncertainty associated with how the simulation model influences the extraction of any B^{**} signal. To study the sensitivity to the simulation, we further varied generation parameters and explored the parameter ranges that are able to describe the data. This study indicated that the most sensitive effect on track distributions was through the “string fragmentation p_T width” ($\sigma_{p_T}^{\text{frag}}$) parameter of PYTHIA, especially when trying to affect the particle p_T distributions. As such, we chose this parameter to define two extremes of the simulation. The “default” PYTHIA simulation (largely tuned to high-energy e^+e^- data) is used as one extreme of the simulation. The other extreme, the “overtuned” simulation, is defined by shifting $\sigma_{p_T}^{\text{frag}}$ from the tuned value by the difference between its

⁴The excess of right-sign hadronization tracks in this picture, along with the contribution from B^{**} decays, is the mechanism of the flavor-tagging technique proposed in Ref. [2].

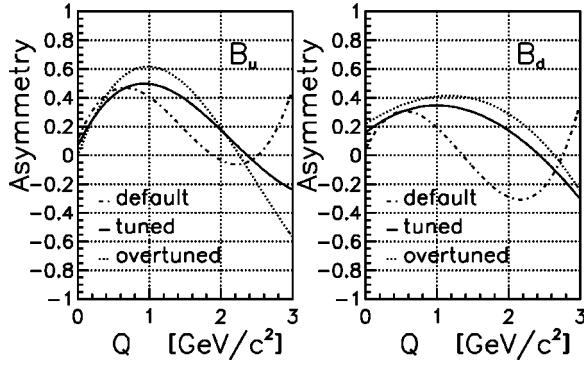


FIG. 9. Asymmetries of the b hadronization particles associated with the two meson types, as produced by the PYTHIA/JETSET Monte Carlo generator. The three sets of curves were produced using different sets of generator parameters (see the text), our nominal description is given by the “tuned” set. The definition of right-sign correlation depends on the flavor of the meson, i.e., positive asymmetry around $B_u(B_d)$ means an excess of $\pi^- (\pi^+)$.

tuned and default values, but in the opposite direction. The values of the other tuning parameters are then determined by readjusting them to obtain the best match—by the same procedures used in the original tuning—between the overtuned simulation and the data. The shift in $\sigma_{p_T}^{\text{frag}}$ between the tuned and the extreme values is more than an order of magnitude larger than the “ 1σ ” uncertainty estimated from the original tuning of the Monte Carlo. We quantify the simulation uncertainty by using this much larger shift to be conservative. The tuned simulation is then used for our nominal description of hadronization particles, and the default and overtuned simulations are used as our 1σ variations.

The predicted asymmetries of the hadronization particles are shown in Fig. 9 for all three sets of parameters. Overall, they have quite different Q distributions, but, significantly, the asymmetries are *not* very sensitive to the Monte Carlo parameters in the *low- Q* region, where we expect the B^{**} signal to be. The divergent behavior at high- Q has little bearing on our result since very few hadronization particles are produced in that region and this corresponds to masses above the region of interest. The asymmetries for charged and neutral B mesons are also seen to behave differently,⁵ and therefore the charged and neutral composition of the various (im-pure) B decay signatures requires careful treatment (Sec. IV A).

In addition to the asymmetry $\mathcal{A}^{\text{HA}}(Q)$ we need the total number distribution $n(Q)$ of the hadronization background

⁵Studies comparing data to simulation [5] indicate that these differences are due to the fact that the hadronization process produces a different $\pi^+/K^+/p$ mix for B^0 compared to B^+ . For example, the generalization of the naive picture of Fig. 8 results in the correlation that a B^+ will be accompanied by a K^- (which we treat as π^-), whereas the B^0 is accompanied by \bar{K}^0 , which is lost to our B^{**} reconstruction. The Monte Carlo simulation predicts that kaons account for nearly two-thirds of the hadronization difference between B^+ and B^0 , and the remainder is caused by protons.

to completely describe the data. In order to further insulate our results from the simulation, we do not rely upon the Monte Carlo to determine this distribution, but we instead used the simulation as a guide to formulate a parametrization of the shape of $n(Q)$ and use the data to fit for the free parameters. We empirically found that

$$n(Q) = \mathcal{N} \exp(-Q/\mathcal{W}) Q^{\mathcal{R}} \quad (2)$$

well described the shapes of the different Monte Carlo simulations. Fits of this parametrization to the simulated distributions indicate that the various subsamples do not prefer significantly different values of \mathcal{R} . This parameter is also highly correlated with the “width” \mathcal{W} in the fits, and varying both \mathcal{R} and \mathcal{W} amounts to overparametrizing the Q distribution. For these reasons, we fix \mathcal{R} to its tuned Monte Carlo value. Furthermore, the widths (\mathcal{W}) of the distributions for charged and neutral B hadronization particles were indistinguishable for a given set of PYTHIA parameters, which we exploit by imposing this as a constraint in our model.

We therefore describe the hadronization Q distributions in the data by the parametrization of Eq. (2) with separate normalizations \mathcal{N}_u and \mathcal{N}_d for charged and neutral mesons, a common width \mathcal{W} , and the fractional excess $\mathcal{A}^{\text{HA}}(Q)$ of right-sign over wrong-sign tracks fixed to the tuned asymmetry distributions in Fig. 9. We do not rely upon the simulation to determine the values of the three $n(Q)$ parameters, rather they are constrained by the data by allowing them to float in the fits of the measured Q distributions when extracting the B^{**} signal in Sec. IV B. We thus reduce our dependence on the specific hadronization model employed in the simulation to the tuned PYTHIA asymmetry dependence, while using the default and the overtuned distributions to estimate the systematic uncertainty due to the asymmetry constraint.

2. Other correlated backgrounds

There remain a few potential backgrounds that are not accounted for so far. The sideband subtractions of the $D^{(*)}$ mass distributions (Sec. III A) remove fake $D^{(*)}$ backgrounds, and the absence of a signal in the wrong-sign ($l^\pm K^\mp$) charm mass distributions (see Fig. 3) means random (possibly fake) leptons paired with real $D^{(*)}$ mesons are rare. Other backgrounds that may be biased toward the correct $l^\pm K^\pm$ correlation are, however, not accounted for by this mass sideband subtraction. There are several physical processes that can mimic the correct correlation and must still be considered. In contrast to the previously described backgrounds, we do not handle these by sideband subtraction, but instead fold in their charge correlated Q distributions as part of the B^{**} fit discussed in Sec. IV.

A significant fraction of B mesons in our sample decay through D^{**} mesons. The pions from subsequent $D^{**} \rightarrow D^{(*)} \pi^\pm$ decays originate at the secondary vertex (see Fig. 2), but some fraction of them will be consistent with having come from the primary vertex and possibly pose as pions from B^{**} decays. The charge of these pions is fully correlated with the B flavor. We do not attempt to reconstruct the D^{**} states, and requiring all candidate tracks to be incompatible with originating from the secondary vertex, signifi-

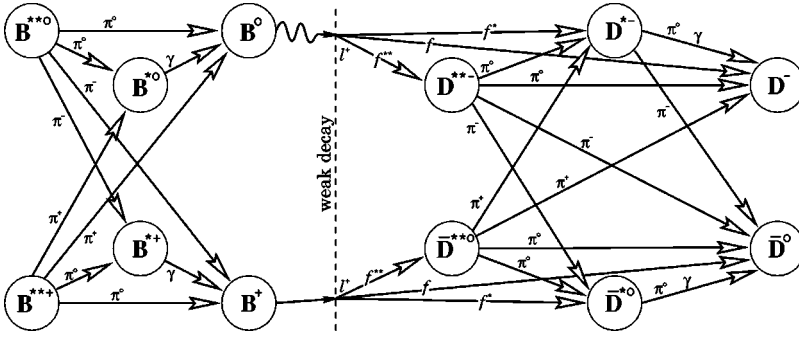


FIG. 10. Diagram of decay transitions contributing to the $l^- D^{(*)}$ samples. The left-hand side portrays the strong decays of excited B mesons to the ground state, the weak semileptonic decays of the $B^{0,+}$ occur in the middle, and the right-hand side shows the decay paths of the various charm mesons that result.

cantly reduces the acceptance for B^{**} candidates. To account for this effect, we add the predicted contribution of the D^{**} pions to the other background distributions when calculating the B^{**} production fraction. The magnitude of this contribution is a function of branching ratios and detection efficiencies.⁶

We also consider the effect of $B_s^{**} \rightarrow B^+ K^-$ decays. Here the kaons—which are not experimentally distinguished from pions—do come from the primary vertex, and therefore contribute to the sample of B^{**} candidates. The Q shape of this contribution is determined from a Monte Carlo calculation using the B_s^{**} mass spectrum predicted in Ref. [9]. For the rate of B_s^{**} production relative to B_s , we use the B^{**} to B production rate scaled by the relative B_s^0 to B_d^0 rates. The B_s^0 to B_d^0 rate is obtained from the measured ratio of the hadronization probabilities $f_s/f_d = 0.30 \pm 0.07$ [20], with a further correction for the $B_s^{**} \rightarrow BK$ feed down. The B^{**} production rate is one of the unknown parameters we are determining, so the B_s^{**} rate is expressed as a function of the floating B^{**} rate as well as the f_s/f_d constraint in the eventual fit. The charged kaon background is only associated with charged B mesons, but B_s^{**} decays also contribute B_d^0 mesons to the samples through $B_s^{**} \rightarrow B^0 K^0$ decays. These effects, which contribute a few percent to the sample size, are also included in the fitting process.

Finally, higher-order heavy flavor production may also contribute $B\text{-}\pi$ candidates to our sample. In particular, gluon splitting to $c\bar{c}$ or $b\bar{b}$ can result in both heavy quarks being near each other and give rise to correlations that may affect the analysis. The $B \rightarrow l^+ D^{(*)} X$ signal can be contaminated by $g \rightarrow c\bar{c}$ when the lepton comes from one charm hadron and the other was reconstructed as a $D^{(*)}$. The correct $l^\pm K^\pm$ charge correlation is present to enter the B sample, but these events rarely pass the selection criteria. Constraints obtained from the data have shown that this $c\bar{c}$ contribution is negligible [5].

On the other hand, $g \rightarrow b\bar{b}$ production is potentially a concern since our procedure for subtracting the underlying event

contribution assumes that there are no decay products of the other b quark—whose charge is correlated with the detected B meson—in the azimuthal region of the detector perpendicular to the B meson direction [i.e., the $1 < |\Delta\phi| < 2$ sideband region of Fig. 6(b)]. In this case the decay products of the b hadron will bias the background subtraction and distort the Q distributions. To account for this effect, we generated events using the PYTHIA program, but reweighted them to agree with the $b\bar{b}$ azimuthal distributions of a next-to-leading-order QCD calculation [21]. From these events, we determined the shape of the charge-correlated Q distributions to model the $g \rightarrow b\bar{b}$ contribution, and add it into the background mix used later in the fit. The rate of this process is not well known; to be conservative we assume it contributes a fraction of 30%, with an uncertainty equal to its full value. We found this uncertainty to have a very small effect on the precision of the final results.

IV. EXTRACTING THE B^{**} PRODUCTION FRACTION

The observed right- and wrong-sign $B\text{-}\pi$ Q distributions (Fig. 7) are composed of weighted averages of different types of Q distributions: those from B^{**} decays, B^+ and B^0 mesons plus hadronization particles, and some residual physics backgrounds (Sec. III B 2). The weights for each type of contribution are determined by the relative detection efficiencies and decay branching ratios of the decay chains involved. Knowledge of these, and the shapes of the various Q distributions, enables one to extract the B^{**} component by comparing these expectations to the observed Q distributions in the data.

To obtain the B^{**} production fraction, we perform a binned χ^2 fit of the ensemble of Q distribution shapes to the background-corrected distributions of Fig. 7. The relative weighting factors of each contribution are, however, complicated by the fact that there are a large number of decay chains contributing varying amounts of “cross talk” between B^0 and B^+ decay signatures. A map of the decay chains is shown in Fig. 10, and the cross talk between the upper and lower halves of the diagram must be unraveled before a B^{**} signal can be extracted.

A. Fitting the Q distributions

To describe the origin and characteristics of $B\text{-}\pi$ candidates, we consider all the possible decay chains that contribute to the B signatures, the sources of all charged particles

⁶We use $f^{**} = 0.36 \pm 0.12$ as the fraction of semileptonic B decays to D^{**} states (derived from CLEO measurements [19]). For the relative branching fraction (P_V) of $D^{**} \rightarrow D^* \pi$, appropriately weighted for B mesons decaying into the four different D^{**} states, we use 0.33 ± 0.28 as previously measured in this same sample [5]. Reconstruction efficiencies are determined by simulation.

that are paired with the B candidates, and importantly, preserve the kinematic and charge correlations between them.

We first consider the hadronization particles, schematically arising on the far left side of Fig. 10. The nature of the hadronization particles is specific to the charge state of the associated $B^{(*)}$ meson.⁷ The Q distribution $n_u(Q)$ describing the hadronization products associated with a bottom meson containing a u quark, is different from the distribution $n_d(Q)$ for the production of one with a d quark. A pure sample of a particular ground-state bottom meson, say B^0 , arises from the production of B , B^* , and B^{**} mesons. The B - π hadronization distribution for directly produced B^0 mesons is $n_d(Q)$, but B^0 mesons arising from $B^{**+} \rightarrow B^0 \pi^+$ decays will follow $n_u(Q)$ instead. This results in one type of a cross talk, i.e., a pure sample of B^0 mesons has a mixture of both $n_d(Q)$ and $n_u(Q)$ hadronization particles. The magnitude of this effect depends upon the B^{**} production fraction that we wish to measure.

The hadronization Q distribution for a pure sample of ground-state B mesons containing an “ x ” light quark is

$$n'_x(Q) = n_x(Q) \alpha_C^x(Q) + n_y(Q) \alpha_I^x(Q), \quad (3)$$

where “ y ” represents the light quark constituent of the cross-talk meson. The coefficients α quantify the magnitude of the cross talk. For example, α_I^x is the fraction of detected B_x mesons that were produced via a B_y^{**} meson and decayed through a charged pion. The subscripts C and I stand for “correct” and “incorrect” association between the type (u or d) of B meson and the hadronization distribution, and $\alpha_C + \alpha_I = 1$. For this particular instance of cross talk, these coefficients can be written

$$\alpha_C = \frac{1 - h^{**} [1 - (1/3) \epsilon_B^{**}]}{1 - h^{**} (1 - \epsilon_B^{**})}, \quad (4)$$

$$\alpha_I = \frac{(2/3) h^{**} \epsilon_B^{**}}{1 - h^{**} (1 - \epsilon_B^{**})}, \quad (5)$$

where h^{**} is the fraction of b quarks hadronizing into light B mesons that are B^{**} states—the number we wish to measure—and ϵ_B^{**} is the efficiency for detecting a B meson produced in B^{**} decay relative to one produced directly in the hadronization process. The latter is a function of the masses of the B^{**} states and is near 80% with our selection requirements. The factor of 2/3 is the fraction of B^{**} mesons that contribute to the cross talk by decaying through a charged pion; we assume it is determined by strong isospin conservation.

The right- and wrong-sign B - π correlations are conveniently handled in terms of asymmetries [Eq. (1)]. Given that the production asymmetry for an x -type meson is $\mathcal{A}_x(Q)$, the asymmetry for the B_x ground-state sample is

$$\mathcal{A}'_x(Q) = \frac{\mathcal{A}_x(Q) n_x(Q) \alpha_C^x - \mathcal{A}_y(Q) n_y(Q) \alpha_I^x}{n_x(Q) \alpha_C^x(Q) + n_y(Q) \alpha_I^x(Q)}. \quad (6)$$

Note that the asymmetries in this equation are *subtracted* in the numerator, which is a direct consequence of the fact that the definition of the right-sign B - π correlation is opposite for the two B meson charge states, B^+ and B^0 .

Equations (3) and (6) provide the means to predict the observed Q distributions for hadronization particles accounting for the cross talk arising from B^{**} decay. We generalize this approach by adding to the weighted averages n' and \mathcal{A}' the contribution from the B^{**} signal. This source has an asymmetry equal to +1 [i.e., $n_{WS}(Q) = 0$] and a shape determined from the Monte Carlo simulation. The shape is dependent upon the masses of the four B^{**} states, but it is strongly distorted by the kinematics of the unobserved neutrino such that most of the structure is washed out. Its α weight is given by the their relative production rate h^{**} and detection efficiency ϵ_B^{**} . Both the production rate and the collective B^{**} mass are the parameters to be determined in this analysis.

At this point we have the Q description for idealized B^0 and B^+ samples. The actual samples of six decay signatures are not pure. Samples derived from B^0 mesons will have an additional cross talk arising from $B^0 - \bar{B}^0$ oscillations. We account for this effect by obtaining a mixing corrected asymmetry \mathcal{A}'' for the B^0 components by multiplying the asymmetry prior to mixing \mathcal{A}' by the factor $(1 - 2\chi_{\text{eff}})$, where χ_{eff} is the probability that a reconstructed neutral B meson has decayed as an antiparticle of the produced one. This probability depends upon the true time-integrated mixing probability as well as the acceptance as a function of the proper time of B decay, and from Monte Carlo calculations it is found to be $21 \pm 1\%$ for our data sample. Note that $B^0 - \bar{B}^0$ oscillations reduce the asymmetry of both the B^{**} signal and the hadronization background, since both are correlated with the B mesons at the time of production, not decay.

The last instance of cross talk to account for is that between the charged and neutral decay chains caused by decays through the excited states of D mesons—the right half of Fig. 10. The final composition of the signal and background is given by formulas like Eqs. (3) and (6), but the coefficients α_C and α_I are calculated in a more involved way from the parameters determining the relative branching ratios of the various decay chains and their relative reconstruction efficiencies following Ref. [5].

Finally the effects of the residual correlated backgrounds of Sec. III B 2 are included. The Q distributions obtained from the simulation are introduced into the weighted average of the asymmetry, with α weights determined by the production, decay, and acceptance of each particular process.

The full expressions describing the weights of the Q distribution due to these various processes are straightforward to derive, but they are somewhat intricate, and we do not reproduce them here as they do not aid the discussion. Some of these weights depend upon the B^{**} fraction we seek. The combined effects of the various contributions to the charge correlated B - π Q distributions are fit to the sideband sub-

⁷We assume that the hadronization particles produced in association with the excited states of B mesons are of the same nature as the ones around the ground state of the same charge.

tracted distributions obtained from the data. The fit is a Q -binned χ^2 fit, performed simultaneously over all decay signatures.

The composition of the background is highly correlated with the B^{**} production fraction h^{**} , which is being measured, as well as with other sample composition parameters, such as f^{**} , χ_{eff} , and P_V , that determine the magnitudes of the three instances of cross talk, i.e., B^{**} decays through charged pions, $B^0 - \bar{B}^0$ oscillations, and decays through excited D meson states. The fit is, therefore, generalized to include χ^2 constraints for these other external parameters. For each of these “constrained floating” parameters, we include a term $\chi_P^2 = [(P^{\text{meas}} - P)/\sigma(P)]^2$ in the full χ^2 , where P^{meas} is the measured value of parameter P , and $\sigma(P)$ is its uncertainty. These values are either taken from measurements in other experiments or determined from our data in a measurement separate from the B^{**} fit [5].

This arrangement of constrained floating parameters aids in the proper estimation of the fit errors. Estimating the systematic errors due to the fixed input parameters by the common practice of varying each of these parameters in turn by 1σ , would overestimate the total uncertainty because of the correlations between the parameters. On the other hand, the correlations are automatically accounted for by letting the parameters float. However, the fitter then returns an uncertainty that is the combination of statistical and systematic effects, σ_{total} . The two classes of uncertainties are separated by repeating the fit with all the constrained floating parameters fixed to the values obtained from the full χ^2 minimization. This reduced fit yields the pure statistical uncertainty σ_{stat} , and, in the Gaussian approximation, we obtain the systematic uncertainty by subtracting in quadrature,

$$\sigma_{\text{syst}}^{\text{corr}} = \sqrt{\sigma_{\text{total}}^2 - \sigma_{\text{stat}}^2}. \quad (7)$$

This systematic uncertainty only includes the effects related to the floating (correlated) fit parameters. Other uncertainties, external to the fit, are added in quadrature as usual.

B. Results

The right- and wrong-sign Q distributions of all six decay signatures are fit simultaneously. The variables that float freely (unconstrained) in the χ^2 fit are the B^{**} production fraction (h^{**}) and the three parameters describing the dashed hadronization background [the B_u and B_d amplitudes \mathcal{N}_u and \mathcal{N}_d , and the common shape parameter \mathcal{W} of Eq. (2)⁸]. In this way we have relied upon the Monte Carlo hadronization model to guide us in selecting a simple parametrization for this background, but the data determines its amplitude and specific shape. The remainder of the parameters float, but are constrained to their externally measured values.

The results of the fit are shown in Fig. 11. The points are the data Q distributions, the dashed curves are the fitted

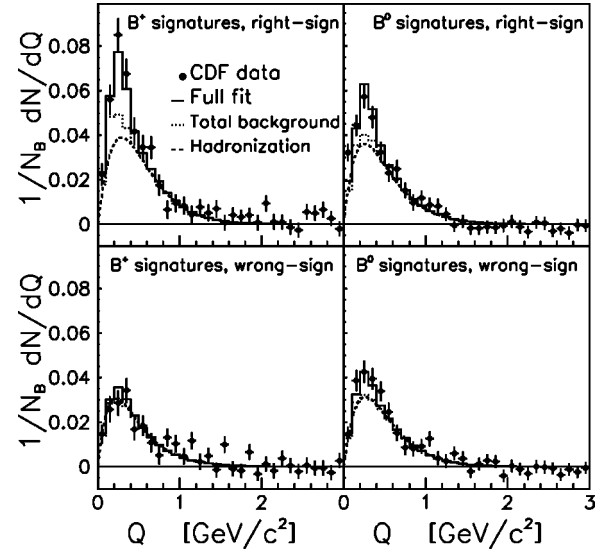


FIG. 11. The sideband subtracted $B - \pi^\pm Q$ distributions of the data (points) compared to the fit results. The dashed curves are the fitted hadronization component, the dotted histograms include all backgrounds, and the solid histograms are the totals including the fitted B^{**} signal.

shapes of the hadronization component, the dotted histograms are the sums of all backgrounds, and the solid histograms are the totals including the fitted B^{**} signal. The complete set of fit parameters is listed in Table IV, including the input constraint values. The fit parameters that determine the sample composition yield the values given in Table V for the coefficients quantifying the $B^0 - B^+$ purity of each decay signature. The cross contamination between these ground-state mesons amounts to no more than 20% in any signature. The fraction of B_s^{**} mesons contributing to the sample, determined by the sample composition fit parameters f_s/f_d , h^{**} , and ϵ_B^{**} (Table IV) is only 3.7%.

From the fit we also learn that the greater right-sign excess seen in B^+ vs $B^0 Q$ distributions—while expected from the greater $B_u^{(*)}$ hadronization excess (see Fig. 9)—is further exaggerated in Fig. 11 by the additional $B^{**} \rightarrow B \pi^\pm$ cross talk, and the asymmetry reduction occurring in B^0 mesons due to $B^0 - \bar{B}^0$ mixing.

Finally, we find the B^{**} production fraction, i.e., the probability that a b quark hadronizing into a light B meson forms an orbitally excited state, to be

$$h^{**} = 0.28 \pm 0.06(\text{stat}) \pm 0.03(\text{syst}). \quad (8)$$

The breakdown of these uncertainties is shown in Table VI. The statistical error can be attributed to several sources: the B meson sample size, the component arising from the statistical limitations in the constraint of the hadronization shape (the “floating hadronization”) to the $ID^{(*)}$ data, and, similarly, from the statistical error in the determination of the “constrained floating” fit parameters that are based on the $ID^{(*)}$ data sample (i.e., P_V and the soft pion efficiency). The systematic uncertainty also has three major classes: the constrained floating parameters of the fit that are determined

⁸As mentioned before, the the power \mathcal{R} in Eq. (2) is fixed to 1.1 (from the simulation) since \mathcal{R} is an excess degree of freedom in the parametrization.

TABLE IV. Fit parameters and results for extracting the B^{**} fraction: The four freely floating parameters, which determine the B^{**} fraction and hadronization shapes, are distinguished by their “input values” being “free.” The remaining parameters are the constrained floating parameters, which have a χ^2 term constraining them in the fit to the listed “input value” by their “input error.” The constrained parameter above the dividing line contributes to the statistical uncertainty of the final result (as it depends upon the data sample). Systematic uncertainties arise from those parameters below the line, i.e., the so-called “external parameters,” which are determined from sources external to this the data sample. The “output error” column is therefore a combination of statistical and a *part* of the systematic uncertainties, as discussed in the text.

Fit parameters		Input value	Input error	Output value	Output error
B^{**} fraction	h^{**}	Free	...	0.28	0.06
B^+ hadronization normalization	\mathcal{N}_u	Free	...	0.95	0.13
B^0 hadronization normalization	\mathcal{N}_d	Free	...	0.92	0.12
Q -hadronization width	\mathcal{W}	Free	...	0.23	0.01
Relative $D^{**} \rightarrow D^* \pi$ rate	P_V	0.33	0.28	0.42	0.24
Reconstruction efficiency for π_s	ϵ_{π_s}	0.74	0.02	0.86	0.07
Relative rate of $B \rightarrow \nu l D^*$ vs $\nu l D$	R_f	2.5	0.6	2.3	0.6
Fraction of $B \rightarrow l X$ decays to D^{**} 's	f^{**}	0.36	0.12	0.32	0.11
Ratio of B^+ to B^0 lifetimes	τ_{B^+} / τ_{B^0}	1.02	0.05	1.03	0.05
Ratio of B_s^0 to B_d^0 hadronization	f_s / f_d	0.30	0.07	0.29	0.07
Effective χ for B^0 mixing	χ_{eff}	0.21	0.01	0.21	0.01
Reconstruction efficiency for B from B^{**}	ϵ_B^{**}	0.763	0.012	0.76	0.01
Reconstruction efficiency for π from B^{**}	ϵ_π^{**}	0.531	0.015	0.53	0.02
Reconstruction efficiency for π from D^{**}	ϵ_D^{**}	0.160	0.009	0.16	0.01
Reconstruction efficiency for B from B_s^{**}	ϵ_s^{**}	0.623	0.025	0.62	0.02
Reconstruction efficiency for K from B_s^{**}	ϵ_K^{**}	0.664	0.064	0.67	0.06

externally to the $lD^{(*)}$ sample (i.e., the “external parameters” listed in the lower portion of Table IV), the systematics associated with the hadronization asymmetry parametrization (i.e., what is left over after accounting for the above statistical uncertainty in its parametrization), and the contribution from gluon splitting. As expected, the largest contribution to the statistical uncertainty comes from floating the shape of the hadronization component in the fit. Similarly, the largest contribution to the systematic uncertainty comes from varying the nominal hadronization asymmetry. This analysis would thus greatly benefit from a more precise means of determining the hadronization background.

To test the hypothesis that background fluctuations could account for our observation, we fit many Monte Carlo generated Q distributions of background only, randomized to represent the statistical power of the data sample. We found that the probability of such a fluctuation to mimic the B^{**} signal is lower than 10^{-6} , including systematic effects.

The experimental resolution does not enable us to disentangle the four B^{**} states, but we may determine an average

mass of the ensemble. We assume the relative production rates of the four mesons are governed by spin counting and use a theoretical prediction of the mass splittings. Templates of the $B^{**}Q$ distributions are constructed for different sets of B^{**} masses. The shape of the distribution is dominated by the smearing caused by missing daughter particles, predominantly the neutrino, and any separation between the four states is largely washed out. For a given hypothesis of the mass splittings, we fit the expected shape of the B^{**} template to the data while collectively varying the masses by stepping through the mass of the narrowest state, the B_1 ($J = 1, j_q = \frac{3}{2}$). The χ^2 's of the fits of the template Q distributions, derived from the splittings calculated in Ref. [9], are shown on the left-hand side of Fig. 12 as a function of $m(B_1)$. The minimum corresponds to

$$m(B_1) = 5.71 \pm 0.02(\text{stat} \oplus \text{syst}) \text{GeV}/c^2, \quad (9)$$

TABLE V. The values of the fraction parameters describing the light quark composition of the reconstructed B signatures. For example, 82.1% of the $lK\pi$ events contain a B_u^+ , and 17.9% a B_d^0 .

Signature	$K\pi$	$K3\pi$	$K\pi\pi$	$K\pi\pi_s$	$K3\pi\pi_s$	$K\pi\pi^0\pi_s$
α_u	0.821	0.826	0.195	0.066	0.072	0.077
α_d	0.179	0.174	0.805	0.934	0.928	0.923

TABLE VI. Uncertainties for the measurement of the B^{**} production fraction h^{**} (see the text).

Statistical uncertainties		
Sample size	-0.029	+0.028
Floating hadronization	-0.048	+0.045
Internal parameters (P_V and ϵ_{π_i})	-0.010	+0.011
Total	-0.057	+0.054
Systematic uncertainties		
External parameters	-0.013	+0.023
Hadronization asymmetry	-0.023	+0.020
NLO $b\bar{b}$ production	-0.005	+0.006
Total	-0.027	+0.031

which is in very good agreement with the predicted value $m(B_1) = 5.719 \text{ GeV}/c^2$. Also shown in Fig. 12 are the corresponding values of h^{**} as a function of $m(B_1)$. There is a relatively small dependence, relative to the uncertainty, of h^{**} on $m(B_1)$ in the immediate neighborhood of the fit minimum.

The quoted uncertainty on the mass includes only the systematic effects accounted for in calculating the production fraction, but does not include the theoretical uncertainty on the shape of the B^{**} peak. If, for example, we vary the splitting between the B_0^* and the B_1 states from the assumed $+19 \text{ MeV}/c^2$ to $+170 \text{ MeV}/c^2$ [8], or to $-109 \text{ MeV}/c^2$ [10–12], while preserving the splittings between two wide and the two narrow states, we observe a shift of -20 and $+20 \text{ MeV}/c^2$ in the respective $m(B_1)$ values obtained.

V. SUMMARY

In conclusion, we have observed the production of orbitally excited B^{**} mesons in $p\bar{p}$ collisions and measured the probability for the creation of an $L=1$ state among the light B mesons to be $0.28 \pm 0.06(\text{stat}) \pm 0.03(\text{syst})$. In addition, assuming a model-dependent set of splittings for the four B^{**} states, we extract the mass of the narrowest B^{**} state to be $m(B_1) = 5.71 \pm 0.02 \text{ GeV}/c^2$.

The main advantage of the method presented in this analysis over other methods published to date, is that we use relatively little input from the Monte Carlo calculation to predict the properties of the largest background, the b hadronization particles. The shape-determining parameters of the hadronization component are left free to float in the fit and only the ratio of abundances of right-sign and wrong-

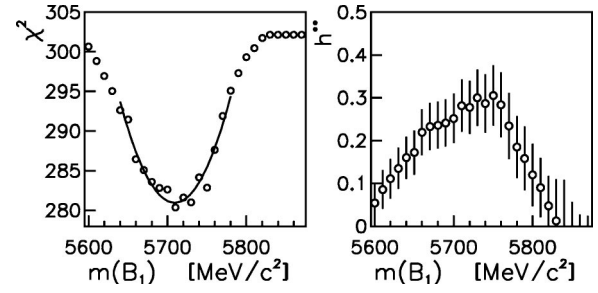


FIG. 12. The χ^2 of the Q distribution fit as a function of the B_1 mass (the narrow $J=1$ state) is shown on the left. The corresponding B^{**} production fraction is shown on the right. The B_1 mass is used to characterize the mass of the B^{**} states, where the splittings between the four states are fixed to the theoretical prediction of Ref. [9].

sign particles is input from the Monte Carlo calculation. The main drawback of this approach is the resulting large statistical uncertainty on the measured B^{**} fraction, since the highly correlated characteristics of the hadronization component are being determined from the same data.

This analysis is a further step toward experimentally unraveling the sources of the tagging power of the B flavor-tagging method used in Refs. [3, 5, 6], and may aid in the construction of better B flavor taggers. Significant improvements in this analysis could be obtained in the future by a better understanding of the hadronization process in the $p\bar{p}$ environment, and distinguishing the narrow from the wide B^{**} resonances. This separation may be possible with the large exclusively reconstructed B samples available in the next Tevatron collider run. Such an effort would be greatly aided by $K-\pi$ separation from a particle identification system.

ACKNOWLEDGMENTS

The authors thank the Fermilab staff and the technical staffs of the participating institutions for their vital contributions. We also thank T. Sjöstrand for his suggestions in tuning PYTHIA/JETSET. This work was supported by the U.S. Department of Energy and National Science Foundation, the Italian Istituto Nazionale di Fisica Nucleare, the Ministry of Education, Science, Sports and Culture of Japan, the Natural Sciences and Engineering Research Council of Canada, the National Science Council of the Republic of China, the Swiss National Science Foundation, the A. P. Sloan Foundation, the Bundesministerium fuer Bildung und Forschung, Germany, and the Korea Science and Engineering Foundation.

- [1] N. Isgur and M. B. Wise, Phys. Lett. B **232**, 113 (1989); **237**, 527 (1990).
- [2] M. Gronau, A. Nippe, and J. Rosner, Phys. Rev. D **47**, 1988 (1993); M. Gronau and J. L. Rosner, *ibid.* **49**, 254 (1994).
- [3] CDF Collaboration, F. Abe *et al.*, Phys. Rev. Lett. **80**, 2057

(1998).

- [4] ALEPH Collaboration, R. Barate *et al.*, Phys. Lett. B **425**, 215 (1998).
- [5] CDF Collaboration, F. Abe *et al.*, Phys. Rev. D **59**, 032001 (1999).

- [6] CDF Collaboration, F. Abe *et al.*, Phys. Rev. Lett. **81**, 5513 (1998); T. Affolder *et al.*, Phys. Rev. D **61**, 072005 (2000).
- [7] E. Eichten, C. Hill, and C. Quigg, Phys. Rev. Lett. **71**, 4116 (1993); FERMILAB-CONF-94/118-T (1994).
- [8] N. Isgur, Phys. Rev. D **57**, 4041 (1998).
- [9] D. Ebert, V. O. Galkin, and R. N. Faustov, Phys. Rev. D **57**, 5663 (1998); **59**, 019902(E) (1999).
- [10] OPAL Collaboration, R. Akers *et al.*, Z. Phys. C **66**, 19 (1995).
- [11] DELPHI Collaboration, P. Abreu *et al.*, Phys. Lett. B **345**, 598 (1995).
- [12] ALEPH Collaboration, D. Buskulic *et al.*, Z. Phys. C **69**, 393 (1996); R. Barate *et al.*, Phys. Lett. B **425**, 215 (1998).
- [13] L3 Collaboration, M. Acciarri *et al.*, Phys. Lett. B **465**, 323 (1999).
- [14] CDF Collaboration, F. Abe *et al.*, Nucl. Instrum. Methods Phys. Res. A **271**, 387 (1988).
- [15] D. Amidei *et al.*, Nucl. Instrum. Methods Phys. Res. A **350**, 73 (1994); P. Azzi *et al.*, *ibid.* **360**, 137 (1995).
- [16] H.-U. Bengtsson and T. Sjöstrand, Comput. Phys. Commun. **46**, 43 (1987).
- [17] P. Avery, K. Read, and G. Trahern, Cornell Internal Note CSN-212, 1985.
- [18] D. Vučinić, Ph.D. dissertation, Massachusetts Institute of Technology, 1999.
- [19] CLEO Collaboration, R. Fulton *et al.*, Phys. Rev. D **43**, 651 (1991).
- [20] Particle Data Group, R. M. Barnett *et al.*, Phys. Rev. D **54**, 1 (1996).
- [21] M. Mangano, P. Nason, and G. Ridolfi, Nucl. Phys. **B373**, 295 (1992).